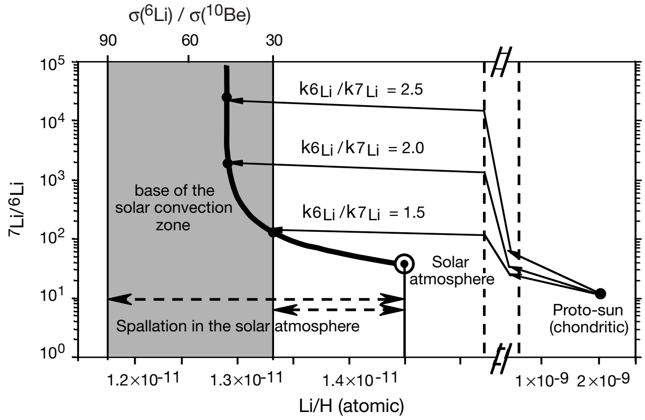

Figure 3 Evolution in the Sun of the ^{7}Li/^{6}Li ratio versus the Li/H ratio. All the calculations are scaled to Li/H $= 1.45 \times 10^{-11}$ and ^{7}Li/^{6}Li $= 31$ for the solar atmosphere. The solid mixing curve shows the compositions at the base of the convection zone compatible with (1) the observed composition of the solar atmosphere and (2) ^{7}Li/^{6}Li $= 2$ for Li produced by spallation. The shaded area indicates the Li/H ratio at the base of the solar convection zone compatible with the measured excess of ^{10}Be in lunar soils[23] (taking spallation cross-section ratios $30 < [\sigma^6\text{Li}/\sigma^{10}\text{Be}] < 90$). In order to satisfy the two constraints derived from the ^{7}Li/^{6}Li and ^{10}Be/H ratios of the solar atmosphere, the deep convecting zone should have ^{7}Li/^{6}Li $\geqslant 150$. Assuming a first-order rate for Li destruction, the ^{7}Li/^{6}Li evolution from the chondritic to the convection-zone value is also shown; this indicates that any destruction-rate ratio $k_{^6\text{Li}}/k_{^7\text{Li}} \geqslant 1.5$ is compatible with the ^{7}Li/^{6}Li ratio (see text).

seems the most likely interpretation of our results, it is important to note that the excess ^{7}Li detected in lunar soils is a solar-wind component (<10 keV) because it is implanted at depths <30 nm (Fig. 1). This implies that the production of the spallogenic components by the flares must be decoupled from their escape to space. The minimum time required to reach the observed $[^6\text{Li/H}]_{\text{spall-S}}$ ratio can be calculated, assuming for simplicity that all ^{6}Li is produced by spallation ($[^6\text{Li/H}]_{\text{spall-S}} = 4.5 \times 10^{-13} = 1.45 \times 10^{-11}/(1 + 31)$) and that no Li destruction occurs at depth in the Sun. We calculate a value of 245 years from the ratio $[^6\text{Li/H}]_{\text{spall-S}}/\Phi_{6\text{Li}}$. The production rate ($\Phi_{6\text{Li}}$) of ^{6}Li is $\Phi_{\text{H}}\sigma(^6\text{Li})[^{16}\text{O} + {}^{12}\text{C}]$, with Φ_{H} the solar proton flux at high energy at the surface of the Sun ($3.2 \times 10^6\ \text{cm}^{-2}\ \text{s}$; ref. 25), $\sigma(^6\text{Li})$ the spallation cross-section for ^{6}Li on ^{16}O and ^{12}C (15 mbarn; ref. 25) and $[^{16}\text{O} + {}^{12}\text{C}]$ the relative solar abundances of carbon and oxygen)^{16}O/H and ^{12}C/H $= 8.5 \times 10^{-4}$ and 3.63×10^{-4}, respectively[2]). According to this calculation, products of spallation reactions accumulate in the Sun's atmosphere for hundreds of years at least. ☐

Received 4 May; accepted 28 September 1999.

1. Reeves, H. in *Origin and Evolution of the Elements* (eds Prantzos, N., Vangioni-Flam, E. & Cassé, M.) 168–197 (Cambridge Univ. Press, 1993).
2. Anders, E. & Grevesse, N. Abundances of the elements: meteoritic and Solar. *Geochim. Cosmochim. Acta* **53,** 197–214 (1989).
3. Herbig, G. H. Lithium abundances in F5-G8 dwarfs. *Astrophys. J.* **141,** 588–609 (1965).
4. Vauclair, S., Vauclair, G. Schatzman, E. & Michaud, G. Hydrodynamical instabilities in the envelopes of main-sequence stars: constraints implied by the lithium, beryllium and boron observations. *Astrophys. J.* **223,** 567–582 (1978).
5. Brun, A. S. & Turck-Chièze, S. in *LiBeB, Cosmic Rays, and Related X- and Gamma Rays* (eds Ramaty, R., Vangioni-Flam, E., Cassé, M. & Olive, K.) 64–72 (ASP Conf. Ser., Vol. 171, Astronomical Society of the Pacific, San Francisco, 1999).
6. Delbourgo-Salvador, P., Malinie, G. & Audouze, J. in *Isotopic Ratios in the Solar System* 267–272 (Toulouse Cepadues-Editions, 1984).
7. Chaussidon, M. & Robert, F. ^{7}Li/^{6}Li and ^{11}B/^{10}B variations in chondrules from the Semarkona unequilibrated chondrite. *Earth Planet. Sci. Lett.* **164,** 577–589 (1998).
8. Borg, J., Dran, J. C., Durrieu, L., Jouret, C. & Maurette, M. High voltage electron microscope studies of fossil nuclear particle tracks in extraterrestrial matter. *Earth Planet. Sci. Lett.* **8,** 379–386 (1970).
9. Geiss, J. Solar wind composition and implications about the history of the Solar system. *Proc. 13th Int. Cosmic Ray Conf.* Vol. 5, 3375–3398 (Univ. of Denver, 1973).
10. Becker, R. H. & Clayton, R. N. Nitrogen abundances and isotopic compositions in lunar samples. *Proc. Lunar Planet Sci. Conf.* **6,** 2131–2149 (1975).
11. Deliyannis, C. P., Demarque, P. & Kawaler, S. D. Lithium in halo stars from standard evolution. *Astrophys. J. Suppl.* **73,** 21–65 (1990).
12. Eugster, O. & Bernas, R. Li, B, Mg and Ti isotopic abundances and search for trapped Solar wind Li in Apollo 11 and 12 material. *Proc. Lunar Planet Sci. Conf.* **2,** 1461–1469 (1971).
13. Ritzenhoff, S., Schröter, E. H. & Schmidt, W. The lithium abundance in sunspots. *Astron. Astrophys.* **328,** 695–701 (1997).
14. Bibring, J. P. *et al.* Ultrathin amorphous coatings on lunar dust grains. *Science* **175**, 753–755 (1972).
15. Keller, L. P. & McKay, D. S. The nature and origin of rims on lunar soil grains. *Geochim. Cosmochim. Acta* **61,** 2331–2341 (1997).
16. Borg, J. *et al.* A Monte Carlo model for the exposure history of lunar dust grains in the ancient Solar wind. *Earth Planet. Sci. Lett* **29,** 161–174 (1976).
17. Reedy, R. O. in *The Ancient Sun* (eds Pepin, R. O., Eddy, J. A. & Merril, R. B.) 365–386 (GCA Suppl. Vol. 13, Lunar and Planetary Institute, Houston, Texas) (Pergamon, 1979).
18. Christensen-Dalsgaard, J., Gough, D. O. & Thompson, M. J. The depth of the Solar convection zone. *Astrophys. J.* **378,** 413–437 (1991).
19. Audouze, J., Boulade, O., Malinie, G. & Poilane, Y. Galactic evolution of the lithium isotopes. *Astron. Astrophys.* **127,** 164–168 (1983).
20. Balachandran, S. C. & Bell, R. A. Shallow mixing in the solar photosphere inferred from revised beryllium abundances. *Nature* **392,** 791–793 (1998).
21. Chaussidon, M. & Robert, F. Nucleosynthesis of ^{11}B-rich boron in the pre-solar cloud recorded in meteoritic chondrules. *Nature* **374,** 337–339 (1995).
22. Smith, V. V., Lambert, D. L. & Nissen, P. E. The ^{7}Li/^{6}Li ratio in the metal-poor halo dwarfs HD 19445 and HD 84937. *Astrophys. J.* **408,** 262–276 (1993).
23. Nishiizumi, K., Caffee, M. W. & Arnold, J. R. ^{10}Be from the active Sun. *Proc. Lunar Planet. Sci. Conf.* **28,** 1027–1028 (1997).
24. Jull, A. J. T., Lal, D. & Donahue, D. J. Evidence for a non-cosmogenic implanted ^{14}C component in lunar samples. *Earth Planet. Sci. Lett.* **136,** 693–702 (1995).
25. Sisterson, J. M., Kim, K., Caffee, M. W. & Reedy, R. C. ^{10}Be and ^{26}Al production in lunar rock 68815: revised production rates using new cross section measurements. *Proc. Lunar Planet. Sci. Conf.* **28,** 1327–1328 (1997).
26. Reeves, H. On the origin of the light elements. *Annu. Rev. Astron. Astrophys.* **12,** 437–467 (1974).
27. Hashizume, K., Marty, B. & Wieler, R. Single grain analyses of the nitrogen isotopic composition in the lunar regolith: in search of the Solar wind component. *Proc. Lunar Planet. Sci. Conf.* **30,** 1567–1568 (1999).

Acknowledgements

We thank J. Audouze, S. Vauclair and R. Reedy for discussions, and G. Huss for contributions to this Letter. This work was supported by INSU-CNRS, CNES and MNHN.

Correspondence and requests for materials should be addressed to M.C. (e-mail: chocho@crpg.cnrs-nancy.fr).

Carbon nanotube intramolecular junctions

Zhen Yao*, Henk W. Ch. Postma*, Leon Balents† & Cees Dekker*

** Department of Applied Sciences and DIMES, Delft University of Technology, Lorentzweg 1, 2628 CJ Delft, The Netherlands*
† Bell Laboratories, Lucent Technologies, Murray Hill, New Jersey 07974, USA

The ultimate device miniaturization would be to use individual molecules as functional devices. Single-wall carbon nanotubes (SWNTs) are promising candidates for achieving this: depending on their diameter and chirality, they are either one-dimensional metals or semiconductors[1,2]. Single-electron transistors employing metallic nanotubes[3,4] and field-effect transistors employing semiconducting nanotubes[5] have been demonstrated. Intramolecular devices have also been proposed which should display a range of other device functions[6–11]. For example, by introducing a pentagon and a heptagon into the hexagonal carbon lattice, two tube segments with different atomic and electronic structures can be seamlessly fused together to create intramolecular metal–metal, metal–semiconductor, or semiconductor–semiconductor junctions. Here we report electrical transport measurements on SWNTs with intramolecular junctions. We find that a metal–semiconductor junction behaves like a rectifying diode with nonlinear transport characteristics that are strongly asymmetric with respect to bias polarity. In the case of a metal–metal junction, the conductance appears to be strongly suppressed and it displays a power-law dependence on temperatures and

applied voltage, consistent with tunnelling between the ends of two Luttinger liquids. Our results emphasize the need to consider screening and electron interactions when designing and modelling molecular devices. Realization of carbon-based molecular electronics will require future efforts in the controlled production of these intramolecular nanotube junctions.

Figure 1a and b display examples of atomic force microscope images of nanotube junction devices. Each nanotube consists of two straight segments, both with measured heights of ~1 nm, connected by a sharp kink of about 40°. In principle, such kinks can originate from two different mechanisms: a pentagon–heptagon (5–7) topological defect pair as illustrated in Fig. 1c, or a local mechanical deformation in a uniform nanotube. Both experiments and simulations[12,13] have shown that a nanotube will elastically deform under a small bending stress, and buckle if the local curvature exceeds a critical value. In this case, a height increase at the buckling point is expected. From our microscope images, however, the kinks appear to be very abrupt, and there seems to be no height increase at the kinks. This suggests that the kinks correspond to the 5–7 defects. Insertion of a pentagon (or heptagon) into the hexagonal carbon network creates a caplike (or saddlelike) curvature. A 5–7 pair will in general lead to a kink (see Fig. 1c). In order to generate a kink of a large angle, the pentagon and heptagon must be placed on the opposite sides of the kink[7]. Further structural evidence for the occurrence of 5–7 pairs comes from a double-kink sample shown in the Supplementary Information.

The nanotube shown in Fig. 1a is lying on three electrodes. The upper straight segment has a two-probe linear resistance of 110 kΩ at room temperature (inset Fig. 2a) with no gate-voltage dependence, indicating that it is metallic[5]. In striking contrast, the current–voltage (*I*–*V*) characteristic across the kink (shown in Fig. 2a) is highly nonlinear and asymmetric, resembling that of a rectifying diode. The current rises sharply above a threshold voltage for a positive bias applied to the upper electrode. There is a small increase in current for large reverse bias. At around zero bias, the junction impedance is immeasurably high. Rectifying behaviour as a possible signature for metal–semiconductor (M–S) heterojunctions was previously observed in a film of entangled SWNTs (ref. 14). However, the junctions were not explicitly observed, and contact with metal electrodes and intertube tunnelling, which can also give rise to the observed behaviour, cannot be excluded. The *I*–*V* characteristics presented here are clearly associated with the kink defect. We have also measured *I*–*V* characteristics for different gate voltages V_g (Fig. 2b). The *I*–*V* curve seems to shift along the voltage axis as a function of V_g (inset Fig. 2b). Upon application of a negative V_g, the *I*–*V* curve becomes increasingly asymmetric. The curve at $V_g = -4$ V shows almost perfect rectifying behaviour up to the largest bias voltage (–4 V) that we have applied. The strong gate modulation demonstrates unambiguously that the lower nanotube segment is semiconducting and that the kink is an M–S heterojunction.

For an isolated nanotube containing an M–S junction, the Fermi energy of the metallic segment is aligned with the middle of the energy gap of the semiconducting segment. The alignment is modified when the sample is connected to metal electrodes.

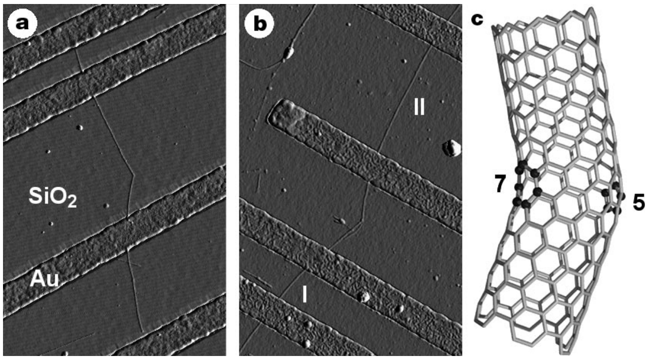

Figure 1 Tapping-mode atomic force microscope amplitude images of examples of nanotube junction devices. **a**, **b**, Nanotubes that contain a single kink of 36° and 41° respectively. We have detected in total four single-kink and one double-kink (see Supplementary Information) samples out of the ~500 devices we have inspected. These kinks can be associated with pentagon and heptagon defects which join two nanotube pieces with different diameters and chiralities. **c**, Illustration of the carbon-bond network of a kink junction constructed between an 'armchair' tube and a 'zigzag' tube, where 5 denotes a pentagon, 7 denotes a heptagon, and the atoms in the pentagon and heptagon are highlighted by dark balls. The nanotube in **a** is on top of three electrodes. Device **b**, with four leads connected, represents the ideal geometry, where both straight segments, I and II, and the kink can be characterized separately. The 250-nm wide, 20-nm-thick titanium-gold electrodes are embedded in SiO_2 with a height difference of less than 1 nm, which minimises the deformation of the nanotubes. This is achieved by standard electron-beam lithography, evaporation and lift-off, combined with an additional step of reactive-ion etching. A highly-doped silicon substrate below SiO_2 is used as a gate to vary the carrier density of the nanotubes. Nanotubes are deposited on top of the electrodes by spin coating of a drop of SWNT suspension in dichloroethane. The two-probe resistance of an individual straight metallic SWNT is typically ≤100 kΩ at room temperature, more than an order of magnitude less than in earlier experiments[3,5] (Z.Y. *et al.*, unpublished results). The low tube-electrode contact resistance proves essential in this work.

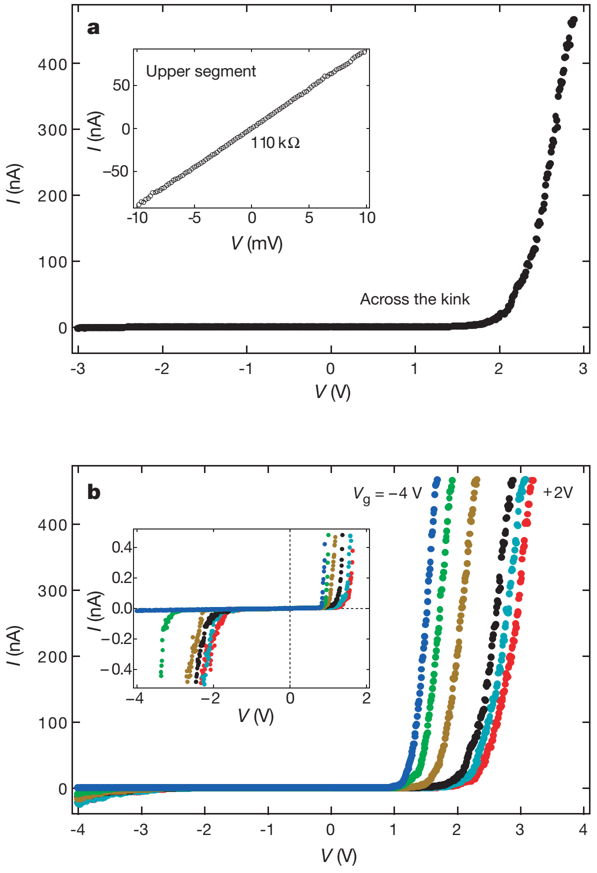

Figure 2 Current–voltage characteristics across the metal–semiconductor junction of Fig. 1a, showing rectifying behaviour. The data are taken at 100 K. The results at room temperature are similar, but the data are noisier. Inset to **a**, the *I*–*V* curve for the upper straight segment measured at room temperature. The low resistance value and the absence of a gate effect indicate that this segment is metallic. In **a**, the gate is grounded. In **b**, the gate voltages from right to left are 2 V, 1 V, 0 V, –1 V, –2 V and –4 V respectively. Inset to **b**, expanded view of the small-current region which shows more clearly the onset of conduction for both bias polarities. The junction resistance around zero bias is >250 GΩ. The strong gate modulation demonstrates convincingly that the kink is a metal–semiconductor heterojunction.

Owing to the higher work function for the metal, both pieces will be hole-doped by the electrodes[1,5]. The difference in electronic structures and screening properties of metallic and semiconducting nanotubes will give rise to different band-bending profiles in the tube segments away from the electrodes and subsequently a Schottky-type barrier at the M–S interface, which may explain the rectifying behaviour across the junction. Further modelling is required to understand the details of the I–V characteristics.

Each of the two straight segments of the sample in Fig. 1b lies on two electrodes, which permits their separate characterization and also two- and four-probe measurements across the kink. Figure 3 shows the temperature (T) dependence of the two-probe conductance (G) measured between different electrodes at zero bias. At room temperature, the resistances of the two straight segments are 56 and 101 kΩ respectively, with no gate-voltage dependence, demonstrating that both are metallic. The resistance across the junction is 608 kΩ, which is much higher. As the temperature decreases, all the conductances decrease monotonically. The conductance across the junction is much more temperature-dependent than that of the two straight segments, and decreases over one order of magnitude as the temperature decreases from 300 K to 50 K. Four-probe and two-probe measurements across the kink give essentially the same conductance value, indicating that the observed temperature dependence is completely dominated by the junction itself.

Although a defect is always expected to degrade the conductance, simple tight-binding calculations, which neglect electron–electron interactions, of the conductance across a metal–metal (M–M) kink junction cannot produce the large suppression seen in our experiments[15]. In Fig. 3 the data are plotted on a double-logarithmic scale. It appears that all the conductances can be fitted with a power-law function of T, $G \propto T^{\alpha}$, which is particularly convincing for the conductance across the junction because of its strong temperature dependence. Power-law behaviour of G versus T was reported recently for metallic ropes of nanotubes[16], and was interpreted as a signature for electron–electron correlations[17,18]. It has been known for decades that electron interactions are of great importance in one-dimensional transport[19]. Electrons form a correlated ground state called Luttinger liquid (LL), in which the tunnelling density of states is suppressed as a power-law function of energy, $\rho(E) \propto E^{\alpha}$. Tunnelling into the end of an LL is more strongly suppressed than into the bulk, that is, the exponent for end tunnelling α_{end} is larger than the exponent for bulk tunnelling α_{bulk}. For an LL connected to three-dimensional reservoirs by tunnel barriers, the tunnelling conductance in the linear-response regime should vary as $G(T) \propto T^{\alpha}$ (for $eV \ll k_{\mathrm{B}}T$, where e is the electron charge and k_{B} is the Boltzmann constant) and the differential conductance $\mathrm{d}I/\mathrm{d}V$ at large bias ($eV \gg k_{\mathrm{B}}T$) should vary as $\mathrm{d}I/\mathrm{d}V \propto V^{\alpha}$. An interesting question arises when a tunnel junction is placed between two LLs (ref. 19). To a first-order approximation, the tunnelling conductance

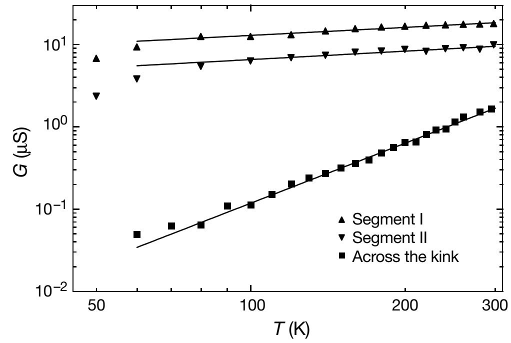

Figure 3 Linear-response two-probe conductances G of segments I and II and across the metal–metal junction of Fig. 1b, plotted against temperature T on a double-logarithmic scale. The data are fitted (solid lines) by the power law, $G(T) \propto T^{\alpha}$, which is associated with the suppression of tunnelling density of states in a Luttinger liquid. The exponents α for the two straight segments are 0.34 and 0.35 respectively. The fit is particularly convincing for the data across the kink. An exponent of 2.2 is obtained, which is consistent with end-to-end tunnelling between two Luttinger liquids. A thermally activated form for transport over a tunnel junction of barrier height U, $G \propto \exp(-U/k_{\mathrm{B}}T)$, does not fit well. For the two straight segments, the overall behaviour is similar to that reported for ropes of nanotubes[16], and is typical for our samples of individual SWNTs with similar conductance values (H. P. *et al.*, unpublished results). The low-temperature deviation from the power law is due to the Coulomb-blockade effect, which sets in when $k_{\mathrm{B}}T$ becomes comparable to the charging energy, $E_{\mathrm{c}} = e^{2}/2C$, needed to put an extra electron onto the nanotube, where C is the total capacitance of the tube.

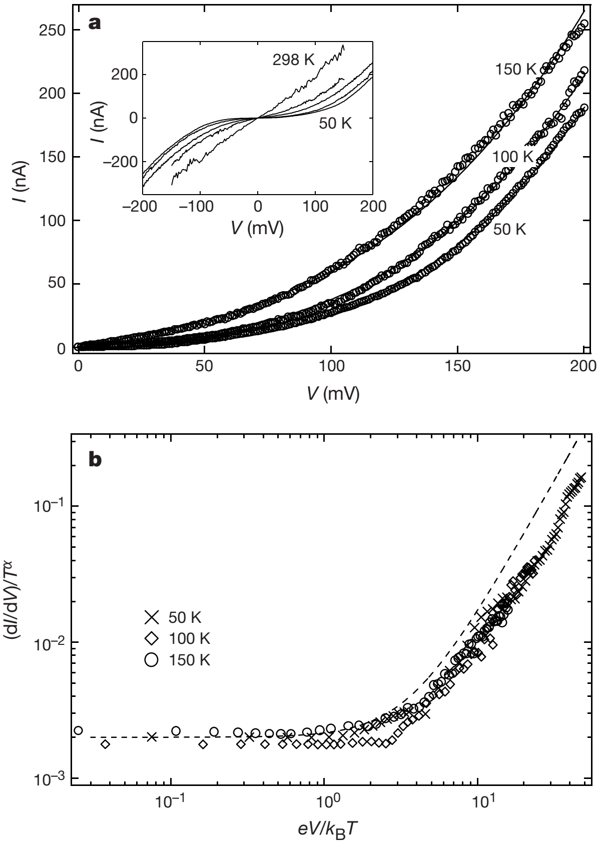

Figure 4 Large-bias transport characteristics measured across the metal–metal junction of Fig. 1b. **a**, Nonlinear I–V characteristics at different temperatures showing consistency with the Luttinger model. The data are fitted (solid lines) by a phenomenological functional form $I = C_1 T^{\alpha} V(1 + C_2(eV/k_{\mathrm{B}}T)^{\alpha})$, where C_1 and C_2 are constants. An exponent of $\alpha = 2.1$ is obtained which is similar to the value from G versus T measurement across the kink. The inset shows I–V curves at temperatures of 298 K, 200 K, 150 K, 100 K and 50 K. **b**, Scaled differential conductance $(\mathrm{d}I/\mathrm{d}V)/T^{\alpha}$ across the junction plotted against $eV/k_{\mathrm{B}}T$, where $\alpha = 2.2$ is obtained from the power-law fit of G versus T across the kink. The data taken at various temperatures appear to collapse onto one curve. $\mathrm{d}I/\mathrm{d}V$ is obtained by numerically differentiating the I–V curves shown in **a**. The dashed line represents the theoretical scaling function expected for the end-to-end tunnelling between two Luttinger liquids. At large bias, the measured conductance is lower than the theoretical prediction. Several factors may be responsible for the deviation. We have assumed that the voltage applied between the two contacts drops entirely across the junction, which is reasonable at small bias. As bias voltage is increased, however, more and more voltage drop will occur at the contacts because tunnelling conductance across the contacts (bulk tunnelling) increases less strongly as a function of voltage than that across the junction (end-to-end tunnelling). This effectively leads to reduced conductance across the junction compared to the case where one assumes a complete voltage drop across the junction. Additionally, the tunnelling amplitude across the junction may be energy-dependent at large bias. If the junction is viewed as a nanometer-sized capacitor, charging it to a few hundred millivolts may lead to a strong electrostatic force which could possibly deform the junction and reduce the transmission.

across the junction is proportional to the product of the end-tunnelling density of states on both sides and therefore still varies as a power law of energy, but with an exponent twice as large as the end tunnelling, that is, $\alpha_{\text{end–end}} = 2\alpha_{\text{end}}$.

Single-wall carbon nanotubes are truly one-dimensional conductors and are thus expected to behave as LLs. The strength of electron interactions is described by the so-called Luttinger parameter g. For non-interacting electrons $g = 1$, whereas for repulsive Coulomb interactions $g < 1$. The exponents α for tunnelling into the bulk and end of a nanotube LL are related to g as $\alpha_{\text{bulk}} = (g^{-1} + g - 2)/8$ and $\alpha_{\text{end}} = (g^{-1} - 1)/4$ respectively[18]. In our experiments, bulk tunnelling is expected for the measurements of the straight segments. Fitting the high-temperature data for the two straight segments yields similar exponents $\alpha = 0.34$ and 0.35, which gives a value of $g \approx 0.22$ using the above expression for bulk tunnelling. This g value agrees with theoretical estimates[17,18] and with that reported for ropes[16] and clearly indicates the strong electron–electron interactions in SWNTs. Having established that both straight segments are LLs, we expect that the conduction process between the middle two contacts takes place via end-to-end tunnelling between the two LLs as well as tunnelling in and out of the two LLs through the contacts. However, the end-to-end tunnelling dominates the energy dependence of the process. Substituting the above g value into $\alpha_{\text{end–end}} = (g^{-1} - 1)/2$, an exponent of 1.8 is expected for the tunnelling conductance across the junction. Fitting the experimental data with a power law yields $\alpha = 2.2$, which is indeed close to this value. This analysis is not based on any presumed g value (which is sample-dependent). The self-consistency of bulk and end-to-end tunnelling thus provides strong evidence for the Luttinger model.

We have also measured large-bias I–V characteristics across the M–M junction at different temperatures, which provide an independent verification of the LL theory. As is evident from Fig. 4a, the I–V curves are nonlinear at all temperatures. The current is expected to increase as $V^{\alpha+1}$ for $eV \gg k_BT$. We consider the differential conductance which, assuming a constant tunnelling amplitude across the junction, is predicted to satisfy a scaling function:

$$\frac{dI}{dV} \propto T^{\alpha}\sinh\left(\frac{eV}{2k_BT}\right)\left|\Gamma\left(1+\frac{\alpha}{2}+i\frac{eV}{2\pi k_BT}\right)\right|^2 \times \left\{\frac{1}{2}\coth\left(\frac{eV}{2k_BT}\right) - \frac{1}{\pi}Im\left[\Psi\left(1+\frac{\alpha}{2}+i\frac{eV}{2\pi k_BT}\right)\right]\right\}$$

Here α is the end-to-end tunnelling exponent and Γ and Ψ are the gamma and digamma functions respectively. For $\alpha = 2$, a good approximation (exact when $\alpha = 2$) of the above expression is given by $dI/dV \propto T^{\alpha}(1 + 3(eV/2\pi k_BT)^{\alpha})$, which clearly shows the expected power-law behaviour at large bias. The expression suggests that if we scale dI/dV by T^{α} and V by T, then curves obtained at different temperatures should all collapse onto one universal curve. This is shown in Fig. 4b for our experimental data. The scaled conductance is constant for small V but crosses over to a power law for $eV/k_BT > 3$. Its behaviour is qualitatively similar to the theoretical scaling function (dashed line) in Fig. 4b. The deviation at large bias may be explained by a reduced voltage drop and/or a reduced tunnelling amplitude across the kink (see Fig. 4 legend). Overall, however, end-to-end tunnelling between two LLs seems to capture the main physics of the observed data. ☐

Received 24 June; accepted 29 September 1999.

1. Wildöer, J. W. G., Venema, L. C., Rinzler, A. G., Smalley, R. E. & Dekker, C. Electronic structure of atomically resolved carbon nanotubes. *Nature* **391,** 59–62 (1998).
2. Odom, T. W., Huang, J., Kim, P. & Lieber, C. M. Atomic structure and electronic properties of single-walled carbon nanotubes. *Nature* **391,** 62–64 (1998).
3. Tans, S. J. *et al.* Individual single-wall carbon nanotubes as quantum wires. *Nature* **386,** 474–477 (1997).
4. Bockrath, M. *et al.* Single-electron transport in ropes of carbon nanotubes. *Science* **275,** 1922–1925 (1997).
5. Tans, S. J., Verschueren, A. R. M. & Dekker, C. Room-temperature transistor based on a single carbon nanotube. *Nature* **393,** 49–52 (1998).
6. Chico, L., Crespi, V. H., Benedict, L. X., Louie, S. G. & Cohen, M. L. Pure carbon nanoscale devices: Nanotube heterojunctions. *Phys. Rev. Lett.* **76,** 971–974 (1996).
7. Lambin, Ph., Fonseca, A., Vigneron, J. P., Nagy, J. B. & Lucas, A. A. Structural and electronic properties of bent carbon nanotubes. *Chem. Phys. Lett.* **245,** 85–89 (1995).
8. Saito, R., Dresselhaus, G. & Dresselhaus, M. S. Tunnelling conductance of connected carbon nanotubes. *Phys. Rev. B* **53,** 2044–2050 (1996).
9. Charlier, J.-C., Ebbesen, T. W. & Lambin, Ph. Structural and electronic properties of pentagon-heptagon pair defects in carbon nanotubes. *Phys. Rev. B* **53,** 11108–11113 (1996).
10. Menon, M. & Srivastava, D. Carbon nanotube "T junctions": Nanoscale metal-semiconductor-metal contact devices. *Phys. Rev. Lett.* **79,** 4453–4456 (1997).
11. Chico, L., López Sancho, M. P. & Muñoz, M. C. Carbon-nanotube-based quantum dot. *Phys. Rev. Lett.* **81,** 1278–1281 (1998).
12. Iijima, S., Brabec, C. J., Maiti, A. & Bernholc, J. Structural flexibility of carbon nanotubes. *J. Chem. Phys.* **104,** 2089–2092 (1996).
13. Yakobson, B. I., Brabec, C. J. & Bernholc, J. Nanomechanics of carbon tubes: Instabilities beyond the linear response. *Phys. Rev. Lett.* **76,** 2511–2514 (1996).
14. Collins, P. G., Zettl, A., Bando, H., Thess, A. & Smalley, R. E. Nanotube nanodevice. *Science* **278,** 100–103 (1997).
15. Chico, L., Benedict, L. X., Louie, S. G. & Cohen, M. L. Quantum conductance of carbon nanotubes with defects. *Phys. Rev. B* **54,** 2600–2606 (1996).
16. Bockrath, M. *et al.* Luttinger-liquid behaviour in carbon nanotubes. *Nature* **397,** 598–601 (1999).
17. Egger, R. & Gogolin, A. Effective low-energy theory for correlated carbon nanotubes. *Phys. Rev. Lett.* **79,** 5082–5085 (1997).
18. Kane, C., Balents, L. & Fisher, M. P. A. Coulomb interactions and mesoscopic effects in carbon nanotubes. *Phys. Rev. Lett.* **79,** 5086–5089 (1997).
19. Fisher, M. P. A. & Glazman, L. I. in *Mesoscopic Electron Transport* (eds Kouwenhoven, L. P., Sohn, L. L. & Schön, G.) 331–373 (Kluwer Academic, Boston, 1997).

Supplementary information is available on *Nature*'s World-Wide Web site (http://www.nature.com) or as paper copy from the London editorial office of *Nature*.

Acknowledgements

We thank R. E. Smalley and co-workers for providing the indispensable single-wall carbon nanotube materials, M. P. Anantram, S. J. Tans and A. A. Odintsov for helpful discussions, V. Meunier for the atomic coordinates used in Fig. 1c, and M. de Jonge and A. van den Enden for experimental assistance. The work was supported by the Dutch Foundation for Fundamental Research on Matter (FOM).

Correspondence and requests for materials should be addressed to C.D. (e-mail: dekker@qt.tn.tudelft.nl).

Design and synthesis of an exceptionally stable and highly porous metal-organic framework

Hailian Li[*], Mohamed Eddaoudi[†], M. O'Keeffe[*] & O. M. Yaghi[†]

Materials Design and Discovery Group, [*] Department of Chemistry and Biochemistry, Arizona State University, Tempe, Arizona 85287-1604, USA
[†] Department of Chemistry, University of Michigan, 930 North University, Ann Arbor, Michigan 48109-1055, USA

Open metal–organic frameworks are widely regarded as promising materials for applications[1–15] in catalysis, separation, gas storage and molecular recognition. Compared to conventionally used microporous inorganic materials such as zeolites, these organic structures have the potential for more flexible rational design, through control of the architecture and functionalization of the pores. So far, the inability of these open frameworks to support permanent porosity and to avoid collapsing in the absence of guest molecules, such as solvents, has hindered further progress in the field[14,15]. Here we report the synthesis of a metal–organic framework which remains crystalline, as evidenced by X-ray single-crystal analyses, and stable when fully desolvated and when heated up to 300 °C. This synthesis is achieved by borrowing ideas from metal carboxylate cluster chemistry, where an organic